Spatio-temporal theory of lasing action in optically-pumped rotationally excited molecular gases

Song-Liang Chua,[1,*] **Christine A. Caccamise,**[2] **Dane J. Phillips,**[3]
John D. Joannopoulos,[4] **Marin Soljačić,**[4]
Henry O. Everitt,[5] **and Jorge Bravo-Abad**[4,6]

[1]*Department of Electrical Engineering and Computer Science, MIT, Cambridge, Massachusetts 02139, USA*
[2]*Deloitte Consulting LLP, Arlington, Virginia 22209, USA*
[3]*Kratos Defense, Huntsville, Alabama 35805, USA*
[4]*Department of Physics, MIT, Cambridge, Massachusetts 02139, USA*
[5]*Army Aviation & Missile RD&E Center, Redstone Arsenal, Alabama 35898, USA*
[6]*Departamento de Física Teórica de la Materia Condensada, Universidad Autónoma de Madrid, E-28049, Madrid, Spain*

*csliang@mit.edu

Abstract: We investigate laser emission from optically-pumped rotationally excited molecular gases confined in a metallic cavity. To this end, we have developed a theoretical framework able to accurately describe, both in the spatial and temporal domains, the molecular collisional and diffusion processes characterizing the operation of this class of lasers. The effect on the main lasing features of the spatial variation of the electric field intensity and the ohmic losses associated to each cavity mode are also included in our analysis. Our simulations show that, for the exemplary case of methyl fluoride gas confined in a cylindrical copper cavity, the region of maximum population inversion is located near the cavity walls. Based on this fact, our calculations show that the lowest lasing threshold intensity corresponds to the cavity mode that, while maximizing the spatial overlap between the corresponding population inversion and electric-field intensity distributions, simultaneously minimizes the absorption losses occurring at the cavity walls. The dependence of the lasing threshold intensity on both the gas pressure and the cavity radius is also analyzed and compared with experiment. We find that as the cavity size is varied, the interplay between the overall gain of the system and the corresponding ohmic losses allows for the existence of an optimal cavity radius which minimizes the intensity threshold for a large range of gas pressures. The theoretical analysis presented in this work expands the current understanding of lasing action in optically-pumped far-infrared lasers and, thus, could contribute to the development of a new class of compact far-infrared and terahertz sources able to operate efficiently at room temperature.

© 2011 Optical Society of America

Report Documentation Page		*Form Approved* *OMB No. 0704-0188*

1. REPORT DATE **MAR 2011**	2. REPORT TYPE	3. DATES COVERED **00-00-2011 to 00-00-2011**
4. TITLE AND SUBTITLE **Spatio-temporal theory of lasing action in optically-pumped rotationally excited molecular gases**		5a. CONTRACT NUMBER
		5b. GRANT NUMBER
		5c. PROGRAM ELEMENT NUMBER
6. AUTHOR(S)		5d. PROJECT NUMBER
		5e. TASK NUMBER
		5f. WORK UNIT NUMBER
7. PERFORMING ORGANIZATION NAME(S) AND ADDRESS(ES) **Massachusetts Institute of Technology (MIT),Research Laboratory of Electronics,Cambridge,MA,02139**		8. PERFORMING ORGANIZATION REPORT NUMBER
9. SPONSORING/MONITORING AGENCY NAME(S) AND ADDRESS(ES)		10. SPONSOR/MONITOR'S ACRONYM(S)
		11. SPONSOR/MONITOR'S REPORT NUMBER(S)

12. DISTRIBUTION/AVAILABILITY STATEMENT
Approved for public release; distribution unlimited

13. SUPPLEMENTARY NOTES

14. ABSTRACT

We investigate laser emission from optically-pumped rotationally excited molecular gases confined in a metallic cavity. To this end we have developed a theoretical framework able to accurately describe both in the spatial and temporal domains, the molecular collisional and diffusion processes characterizing the operation of this class of lasers. The effect on the main lasing features of the spatial variation of the electric field intensity and the ohmic losses associated to each cavity mode are also included in our analysis. Our simulations show that, for the exemplary case of methyl fluoride gas confined in a cylindrical copper cavity, the region of maximum population inversion is located near the cavity walls. Based on this fact, our calculations show that the lowest lasing threshold intensity corresponds to the cavity mode that, while maximizing the spatial overlap between the corresponding population inversion and electric-field intensity distributions, simultaneously minimizes the absorption losses occurring at the cavity walls. The dependence of the lasing threshold intensity on both the gas pressure and the cavity radius is also analyzed and compared with experiment. We find that as the cavity size is varied, the interplay between the overall gain of the system and the corresponding ohmic losses allows for the existence of an optimal cavity radius which minimizes the intensity threshold for a large range of gas pressures. The theoretical analysis presented in this work expands the current understanding of lasing action in optically-pumped far-infrared lasers and, thus, could contribute to the development of a new class of compact far-infrared and terahertz sources able to operate efficiently at room temperature.

15. SUBJECT TERMS

16. SECURITY CLASSIFICATION OF:			17. LIMITATION OF ABSTRACT	18. NUMBER OF PAGES	19a. NAME OF RESPONSIBLE PERSON
a. REPORT **unclassified**	b. ABSTRACT **unclassified**	c. THIS PAGE **unclassified**	**Same as Report (SAR)**	**17**	

References and links

1. T. Y. Chang and T. J. Bridges, "Laser actions at 452, 496, and 541 μm in optically pumped CH_3F," Opt. Commun. **1**, 423–426 (1970).
2. T. K. Plant, L. A. Newman, E. J. Danielewicz, T. A. DeTemple, and P. D. Coleman, "High power optically pumped far infrared lasers," IEEE Trans. Microwave Theory Tech. **MT22**, 988–990 (1980).
3. W. H. Matteson and F. C. De Lucia, "Millimeter wave spectroscopic studies of collision-induced energy transfer processes in the $^{13}CH_3F$ laser," IEEE J. Quantum Electron. **19**, 1284–1293 (1983).
4. M. S. Tobin, "A review of optically pumped NMMW lasers," Proc. IEEE **73**, 61–85 (1985).
5. P. K. Cheo (ed.), *Handbook of Molecular Lasers* (Marcel Dekker, Inc., 1987), pp. 495–569.
6. H. O. Everitt, D. D. Skatrud, and F. C. De Lucia, "Dynamics and tunability of a small optically pumped CW far-infrared laser," Appl. Phys. Lett. **49**, 995–997 (1986).
7. R. I. McCormick, H. O. Everitt, F. C. De Lucia, and D. D. Skatrud, "Collisional energy transfer in optically pumped far-infrared lasers," IEEE J. Quantum Electron. **QE-23**, 2069–2077 (1989).
8. H. O. Everitt and F. C. De Lucia, "A time-resolved study of rotational energy transfer into A and E symmetry species of $^{13}CH_3F$," J. Chem. Phys. **90**, 3520–3527 (1989).
9. H. O. Everitt and F. C. De Lucia, "Rotational energy transfer in CH_3F: The $\Delta J = n$, $\Delta K = 0$ processes," J. Chem. Phys. **92**, 6480–6491 (1990).
10. R. L. Crownover, H. O. Everitt, D. D. Skatrud, and F. C. DeLucia, "Frequency stability and reproductibility of optically pumped far-infrared lasers," Appl. Phys. Lett. **57**, 2882–2884 (1990).
11. D. Dangoisse, P. Glorieux, and J. Wascat, "Diffusion and vibrational bottleneck in optically pumped submillimeter laser," Int. J. Infrared Milimeter Waves **2**, 215–229 (1981).
12. J. O. Henningsen and H. G. Jensen, "The optically pumped far-infrared laser: Rate equations and diagnostic experiments," IEEE J. Quantum Electron. **QE-11**, 248–252 (1975).
13. R. J. Temkins and D. R. Cohn, "Rate equations for an optically pumped, far-infrared laser," Opt. Commun. **16**, 213–217 (1976).
14. H. O. Everitt, "Collisional Energy Transfer in Methyl Halides," PhD Thesis (Department of Physics, Duke University, 1990).
15. H. O. Everitt and F. C. De Lucia, "Rotational energy transfer in small polyatomic molecules," in *Advances in Atomic and Molecular Physics* (Academic Press, 1995), Vol. 35, pp. 331–400.
16. L. E. Reichl, *A Modern Course in Statistical Physics* (John Wiley & Sons Inc., 1998).
17. A. E. Siegman, *Lasers* (Univ. Science Books, 1986).
18. R. Bansal (ed.), *Handbook of Engineering Electromagnetics* (Marcel Dekker, Inc., 2004).
19. I. Shamah and G. Flynn, "Vibrational relaxation induced population inversions in laser pumped polyatomic molecules," Chem. Phys. **55**, 103–115 (1981).
20. A. Yariv and P. Yeh, *Photonics: Optical Electronics in Modern Communications* (Oxford University Press, 2007).
21. S. L. Chua, Y. D. Chong, A. D. Stone, M. Soljačić, and J. Bravo-Abad, "Low-threshold lasing action in photonic crystal slabs enabled by Fano resonances," Opt. Express **19**, 1539–1562 (2011).

1. Introduction

It has been forty years since the pioneering work of Chang and Bridges [1] demonstrated generation of submillimeter radiation via stimulated emission from optically-pumped methyl fluoride (CH_3F) gas. Since then, a rich spectrum of laser lines through the 50 μm – 2 mm wavelength region have been obtained from a variety of different molecular gases [2–10]. These developments have made this class of lasers—usually referred to as optically-pumped far infrared (OPFIR) lasers—a central resource for many scientific and technological applications. The physical mechanism underlying the operation of conventional OPFIR lasers has also been extensively studied in past decades [2–15]. In essence, the gain in these systems derives from an optically-driven population inversion between two rotational states in an excited vibrational level of a gas molecule; the laser emission frequency is determined by the frequency of the transition between these two rotational states. The feedback mechanism enabling laser action is often provided by designing the cavity, in which the molecular gas is confined, to act as a one-dimensional Fabry-Perot resonator for the emitted laser frequency.

However, although research on conventional OPFIR lasers is generally considered as a mature field, some central challenges remain for the ultimate application of this technology, such as low efficiency, poor tunability, or limited capability of integration into a compact platform. More than two decades ago it was shown [6] that some of the aforementioned drawbacks can

be overcome by considering the active role that high-energy vibrational states play in the laser operation (previous approaches assumed that the populations of those vibrational states were negligible). These findings demonstrated the feasibility of developing OPFIR lasers able to operate at large pressures (larger than the pressure cut-off determined by the so-called vibrational bottleneck [6,7]) and featuring volumes up to four orders of magnitude smaller than those characterizing typical OPFIR lasers. The advent of quantum cascade lasers to replace CO_2 pump lasers may combine to produce truly compact submillimeter-wave laser sources in the near future.

Surprisingly, despite their great promise, up to date there has been limited interest in further exploring the potential of these discoveries [6] for the development of a novel class of compact far-infrared and terahertz (THz) sources able to operate efficiently at room temperature. In order to do that, it is critical to develop a complete theoretical understanding of the physical mechanisms underlying lasing action in the considered systems. The purpose of this paper is to present such a theoretical analysis. Specifically, we introduce a theoretical framework which generalizes previous works in this area to allow for a realistic description of the spatio-temporal dynamics characterizing the molecular collisional and diffusion processes occurring in the considered OPFIR lasers. Importantly, the effect on the main laser features of both the electric-field (E-field) intensity distribution inside the metallic cell and the ohmic losses associated with the penetration of the E-field inside the metallic walls are also included in our theoretical approach. As we show in this work, both effects are particularly important for a realistic description of the operation of compact OPFIR lasers based on a metallic cavity which waveguides the emitted laser frequency.

Using this theoretical framework, we perform a detailed numerical analysis of laser emission from optically pumped methyl fluoride (CH_3F) gas confined in a cylindrical copper cavity, and find that the model compares well against experimental results. Our calculations show that, for this exemplary system, the region of maximum population inversion concentrates near the cavity walls. The outcome of these calculations also implies that, as a consequence of this population inversion distribution, the lowest threshold intensity corresponds to the cavity mode whose E-field intensity profile presents an optimal spatial overlap with the population inversion distribution, while at the same time, the ohmic losses associated to that cavity mode are minimized. In the case of the considered cylindrical cavity both features are satisfied by the TE_{01} mode. We also analyze how the threshold intensity depends on the gas pressure and the cavity radius. The results from these simulations are explained in terms of the corresponding variation of the overall gain of the system and the ohmic losses associated with the lowest threshold mode. Remarkably, we predict that as the cavity size is varied, the interplay between both factors yields an optimal value of the cavity radius for which the threshold intensity is minimized for a large range of gas pressures.

The paper is organized as follows. Section 2 discusses the theoretical model used throughout this paper. Section 3 presents a detailed analysis of lasing action in the considered molecular gas lasers. Finally, in Section 4 we provide a set of conclusions of this work.

2. Theoretical framework

We start by introducing the theoretical model used to describe the molecular dynamics of the considered optically-pumped polyatomic molecular gases. Fig. 1 illustrates the energy level diagram and the different energy transfer mechanisms that form the basic structure of our model. In the following, we describe each of the processes sketched in Fig. 1 and show how to quantify them using experimentally measured parameters. Before starting this analysis, we point out that the theoretical approach presented here is an extension of previous studies on methyl fluoride CH_3F [6, 7] in order to account for the spatial variations and diffusion of the collisional pro-
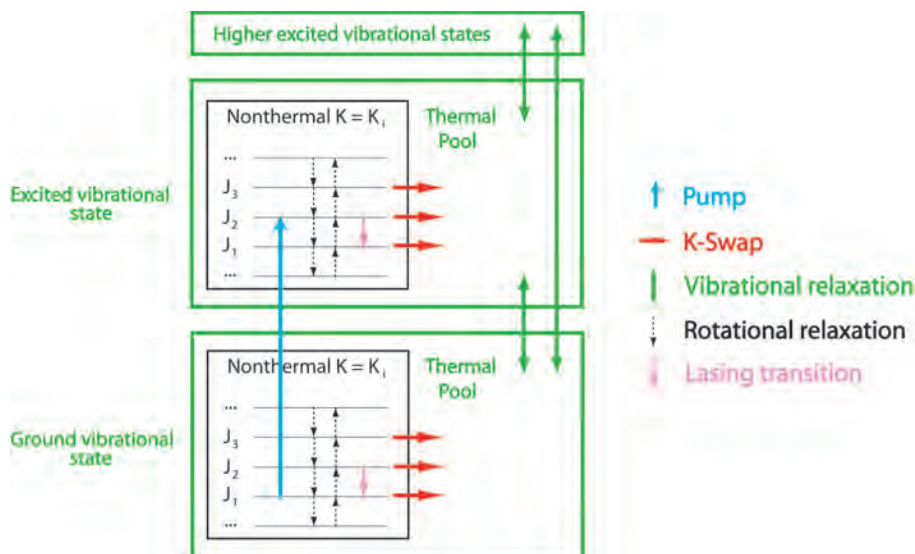
Fig. 1. Schematic diagram of the general model used to describe the dynamics of a OPFIR molecular gas. Details on each process labeled are described in the text.

cesses. We also point out that although for demonstration the model is applied to the case of methyl-halide gases, our theoretical analysis can be easily generalized to most OPFIR systems, both pulsed and CW, and operating over a wide range of experimental conditions utilizing an appropriate gas that satisfied the desired pumping and lasing transition frequencies [15].

The experimentally-motivated thermal pool concept has been previously introduced in OPFIR laser models [3, 7, 8, 15]. In the case of molecules, a thermal pool is observed to be a collection of rotational states that are in thermal equilibrium, and thus, are populated according to a Boltzmann distribution at the operating temperature. Such equilibrium may be attained, for instance, due to the fast relaxation rates among the levels. However, the total population of these pools varies through the flow of energy governed by the collisional and diffusive processes shown in Fig. 1. This fortuitous consolidation of numerous rotational levels into a small number of pools makes numerical simulation tractable, and more importantly, makes rotational energy transfer studies possible in the first place. In the particular case of methyl halides, there exist two thermal pools for each vibrational state, corresponding to the two symmetry types ($A-$ and $E-$type), but without loss of generality they will be combined here to describe CW OPFIR laser operation at low pressure [8]. In addition, all other higher vibrational states that are not connected by the pump are also modeled as pools. This inclusion is important at high pressure and pump intensity since it provides an additional channel through which molecules from the excited vibrational state may be transferred out, and hence, reduces the absorption on the corresponding FIR lasing transition (represented as the pink arrow in the excited state of Fig. 1).

At the relatively low pressure regime considered in this paper, molecules are returned to the ground thermal pool from the pools of the excited and higher excited states, shown as green arrows in Fig. 1, primarily by colliding with the walls of the cavity in which the molecular gas is confined. Unlike molecule-molecule de-excitation processes, these involve diffusion through the gas towards the wall where their rates of occurrences decrease with pressure, and can be defined as $k_{\text{wall}} = v\lambda_{\text{MFP}}/R^2$ [16]. λ_{MFP} is the pressure-dependent mean free path and v is the average relative velocity between molecules. At very low pressure (or equivalently, within λ_{MFP}

from the cavity walls), the transport mechanism changes from diffusion to ballistic and the rate becomes pressure-independent so that $k_{\text{direct}} = v_{\text{abs}}/R$, with v_{abs} defined to be the average absolute velocity of a molecule. It is clear from these expressions that the wall rates are very different across the cavity, and we explicitly account for this spatial variation in our numerical simulations. On the other hand, the vibrational relaxation between the excited and higher excited pools can be dominated by molecule-molecule collisions, in which case, the transition rates between them are $k_{\text{exc}} = N_{\text{tot}} v \sigma_{\text{exc}}$. Here, N_{tot} is the total density of molecules and σ_{exc} is the collision cross section measured from experiments.

Non-equilibrium among rotational and vibrational states in the model is solely introduced by the pump (i.e. the blue arrow in Fig. 1), and the resulting nonthermal distribution of population in some of the rotational levels can no longer be considered part of the thermal pool but must be modeled individually. These nonthermal states, illustrated in Fig. 1 as level J_1, J_2... etc. in each vibrational state, only exist in states that are of the same symmetry type and vibrational state as those connected by the pump. The total population of any state J_i (i.e. N_{tot,J_i}) is simply the sum of its nonthermal and thermal parts, $N_{\text{tot},J_i} = N_{J_i} + f_{J_i} N_{\text{pool}}$, where f_{J_i} is the fraction of the total pool population N_{pool} in state J_i, and N_{J_i} is the amount the state population differs from rotational thermal equilibrium because of the pump. Note that N_{J_i} can be positive (excited vibrational state) or negative (ground vibrational state).

In general, the pump will create significant non-equilibrium not only in the states that it directly connects, but also in those adjacent to it. To account for this, our numerical model allows one to include as many rotational states as are necessary to model such a pump-induced non-equilibrium accurately. Generally, the number of J states to include depends on the ratio of the dipole-dipole rate to the K-swap rate (see end of paragraph for the description of these two processes) — the slower the K-swap rate, the more J levels one needs to consider. As already pointed out, the total population of any nonthermal state in this model is the combined population from both the nonthermal and thermal contributions, but since the thermal pools are in rotational equilibrium, the rotational relaxations, shown as black arrows in Fig. 1, are only modeled for the nonthermal population. In methyl fluoride, the rotational nonthermal processes are primarily dipole-dipole collisions whose rates are computed from the dipole-dipole collision cross section σ_{DD} measured from experiments [9]. Note that their allowed transitions are restricted to $\Delta J = \pm 1$ at the same $K = K_i$ as the pumping transition. Lastly, the K-swap process [8] (i.e. the red arrows in Fig. 1) allows population to be transferred out of nonthermal states into the rest of the rotational levels within the same thermal pool, and its rate constant can again be measured experimentally. The K-swap collisional processes (which encompass the $\Delta K = 3n$ process and the V-swap process [8, 15] when the $A-$ and $E-$symmetry thermal pools are combined as they are here) convert the nonthermal molecules to thermal molecules but not vice versa, and thus, allowing the nonthermal states to return to zero when the pump is turned off.

All of the aforementioned energy transfer mechanisms except K-swap include reverse processes which account for the appropriate degeneracy of the upper and lower levels so that microscopic reversibility is satisfied. Moreover, spatial diffusion of the molecules within the cavity, though a relatively slow process, is also included in order to account for the molecular gas dynamics within the cavity. The pump transition rate, assuming a cylindrical waveguide cavity, is determined from $R_{\text{pump}} = \alpha P_{\text{pump}} / \pi R^2 N_{\text{tot}} f_{\text{low}} h \nu_{\text{IR}}$, where P_{pump} is the pump power, $f_{\text{low}} = f_{J_1}$ is the fraction of molecules in the lower ro-vibrational state J_1 (as depicted in Fig. 1), ν_{IR} is the pump infrared frequency, and α, which takes into account both Doppler broadening and mismatch between pump and absorption lines, measures the gas' ability to absorb the infrared radiation. Hence, pump transition rate may be increased by reducing R, increasing P_{pump}, or decreasing ν_{IR}. The last of these, however, is constrained by the need to match the frequency

of the laser line with that of a ro-vibrational transition in the molecules, and in general, cannot be varied at will. Using such an implementation, our model accommodates both CW and pulsed pumping with arbitrary spatial profiles.

Lastly, we describe the various processes in the model via rate equations, within the rate-equation approximation [17]. The most general rate description of a rotational level would include rotational relaxation terms due to dipole-dipole collisions among the non-thermal J levels, terms representing the pumping mechanism, K-swapping terms that allow flow of molecules out of the non-thermal levels (with equilibrating effects on non-thermal levels), and the stimulated emission terms at the FIR wavelength. Since we are interested in the steady state distribution of molecules across the cavity, spatial diffusion terms are also added to the rate equations describing each levels. Stimulated and spontaneous transitions at the lasing wavelength can, however, be neglected in the rate equations when operated near the threshold if the spontaneous emission lifetime, τ_{spont}, is relatively longer than all other transition lifetimes in the considered system. In methyl fluoride, for instance, τ_{spont} is on the order of $10s$ or more. In contrast, the next longest lifetime in the model occurs for the vibrational relaxation terms and yet, has lifetime on the order of $1 \times 10^{-3}s$ or less. The relative magnitude of these radiative terms involving τ_{spont} in the rate equations are further diminished by the fact that only a fraction of these transitions contributes to the desired laser mode, especially when the cavity is large. With that, the rate equation describing the molecular density of J_2 level in the excited vibrational state (i.e. $N_{J_2}^{\text{exc}}$) of Fig. 1 is given by

$$\frac{\partial N_{J_2}^{\text{exc}}(\mathbf{r},t)}{\partial t} = -R_{\text{pump}}(\mathbf{r},t)\Delta N_{\text{pump}}(\mathbf{r},t) - N_{J_2}^{\text{exc}}(\mathbf{r},t)\sum_{i=1}^{3}\frac{1}{\tau_{J_2,i}} + \sum_{j=1}^{2}\frac{N_j^{\text{exc}}(\mathbf{r},t)}{\tau_{j,J_2}}$$
$$+ D\nabla^2 N_{J_2}^{\text{exc}}(\mathbf{r},t) \tag{1}$$

where $\Delta N_{\text{pump}}(\mathbf{r},t) = N_{\text{tot},J_2}^{\text{exc}}(\mathbf{r},t) - g_{J_2}^{\text{exc}} N_{\text{tot},J_1}^{\text{grd}}(\mathbf{r},t)/g_{J_1}^{\text{grd}}$ with $N_{\text{tot},J_1}^{\text{grd}}$ being the *total* molecular density of the level J_1 in the ground vibrational state after accounting for the nonthermal density and the contribution from the corresponding fraction of the thermal pool, and $g_J^{\text{grd}} = 2J + 1$ is the degeneracy of the ground state J^{th} level. Similar definitions hold for $N_{\text{tot},J_2}^{\text{exc}}$ and g_J^{exc}. $\tau_{J_2,i}$ for $i = 1,2,3$ is the decay lifetime out of $N_{J_2}^{\text{exc}}$ to the two adjacent rotational levels and also the thermal pool. τ_{j,J_2} for $j = 1,2$ represents the decay into $N_{J_2}^{\text{exc}}$ from its two adjacent levels $N_{J_1}^{\text{exc}}$ and $N_{J_3}^{\text{exc}}$. Finally, D is the diffusion constant given by the product of the molecule velocity and mean free path. In the same way, the thermal pool equation has terms from the K-swap and spatial diffusion processes, as well as vibrational relaxations due to molecule-molecule collisions and diffusion to wall. The equation describing the excited vibrational pool in Fig. 1 is then given by

$$\frac{\partial N_{\text{pool}}^{\text{exc}}(\mathbf{r},t)}{\partial t} = -N_{\text{pool}}^{\text{exc}}(\mathbf{r},t)\sum_{k=1}^{2}\frac{1}{\tau_{\text{exc},k}(\mathbf{r})} + \sum_{n=1}^{2}\frac{N_{\text{pool}}^{n}(\mathbf{r},t)}{\tau_{n,\text{exc}}(\mathbf{r})} + \sum_{m=1}^{m_0}\frac{N_{J_m}^{\text{exc}}(\mathbf{r},t)}{\tau_{J_m}^{\text{swap}}}$$
$$+ D\nabla^2 N_{\text{pool}}^{\text{exc}}(\mathbf{r},t) \tag{2}$$

The first two terms relate to the vibrational relaxations among the thermal pools, where $\tau_{\text{exc},k}(\mathbf{r})$ for $k = 1,2$ is the decay lifetime from the excited thermal pool to the ground and higher excited pools, while $\tau_{n,\text{exc}}(\mathbf{r})$ is the reverse. As noted earlier, the values of these diffusive lifetimes depend on their distances from the cell wall. $\tau_{J_m}^{\text{swap}}$ for $m = 1,2,\ldots,m_0$ in the third term is the lifetime of the transition from each of the m_0 rotational levels to the excited pool due to the K-swap molecule-molecule collision process. As in Eq. (1), the last term represents spatial diffusion. Similar equations to Eq. (1) and Eq. (2) are used to represent every nonthermal level or thermal pool that contributes to the lasing action, which in turn depends on their degree of non-equilibrium caused by the pump (see Appendix). This way, the complete set of rate equations

describing our laser system obeys the diffusion equation $\partial N_{tot}(\mathbf{r},t)/\partial t = D\nabla^2 N_{tot}(\mathbf{r},t)$, and so, conserves the total molecular density.

In our simulations, we consider only the immediate nonthermal levels adjacent to the pumped levels and initialize the density of molecules in the thermal pools according to a Boltzmann-distributed partition based on their respective vibrational energies. The non-thermal J_i levels are set equal to zero before any pumping occurs. The set of equations is then evolved in time until steady state is reached, allowing the temporal development of the lasing action to be tracked.

Laser action in this class of OPFIR molecular gas lasers is obtained as follows: Pumping is achieved with a line-tunable laser (e.g. CO_2 laser) which excites molecules from a specific rotational level in the ground vibrational state into a specific rotational level in an excited vibrational state. Because the excited vibrational level is comparatively empty, these photo-excited molecules create a population inversion between the pumped rotational state and the one immediately below it. This leads directly to stimulated emission between rotational states in the excited vibrational state. These photo-excited non-equilibrium molecules are subsequently rotationally and vibrationally relaxed to the ground state through collisions with other molecules and with the chamber walls, respectively.

The population inversion responsible for lasing exists as long as the pump-induced difference in nonthermal population between the upper and lower state $N_{J_i} - N_{J_i-1}$ is greater than the difference in the corresponding pool-contributed thermal populations $(f_{J_i} - f_{J_i-1})N_{pool}$ for those states. As the pressure grows, the pool molecules have an increasingly difficult time reaching the walls and de-exciting; thus, the thermal contribution from the pool increasingly quenches the non-thermal population inversion. Pool quenching creates the vibrational bottleneck that was once believed to limit OPFIR laser operation to low pressures regardless of pump intensity. However, it is now understood that as the excited vibrational state thermal pool fills, near resonant collisions among its constituents can excite molecules to even higher-lying vibrational levels, thereby providing an alternate relaxation pathway [6]. Therefore, the pressure at which vibrational bottleneck occurs for a given laser geometry depends on the pump intensity. By concentrating on low pressure operation in this manuscript, these additional pathways may be ignored to simplify the analysis without affecting the generality of the results.

When molecules are photo-excited from the ground vibrational state to an excited state, two types of population inversion can be induced, and lasing arises from each. The first is the primary lasing transition already described between the pumped rotational state in the excited vibrational level and the rotational state below it. The second is the refilling transition between the IR pump depleted rotational state in the ground vibrational level and the rotational state above it. When the pump is eventually turned off, the K-swap process allows equilibrium conditions in the molecules to be restored. In the following illustration of this theoretical approach, without loss of generality, we present results only for the primary lasing transition.

3. Results and discussion

Figure 2(a) illustrates the setup of the OPFIR laser system considered in this section. A cylindrical waveguide resonator of length L_{cell} and radius R is filled with a suitable gas that lases at the desired THz frequency, while pump power at a much higher IR frequency enters the system from the front window. Depending on the reflectivities of the front and back windows at THz, lasing output power can then escape from the cavity via both channels. In order to compare our numerical calculations with past experimental results, the cavity modeled in the following simulation has length $L_{cell} = 12 \ cm$ and front window reflectivity $\Gamma_{front} = 0.96$. The back window is opaque (i.e. $\Gamma_{back} = 1$). Furthermore, R is varied across a range of commercially available values from the smallest possible before modal cutoff at $0.08 \ cm$ to $1 \ cm$. The cavity is then filled with an isotopic isomer of methyl fluoride gas, $^{13}CH_3F$, where a total of six rota-
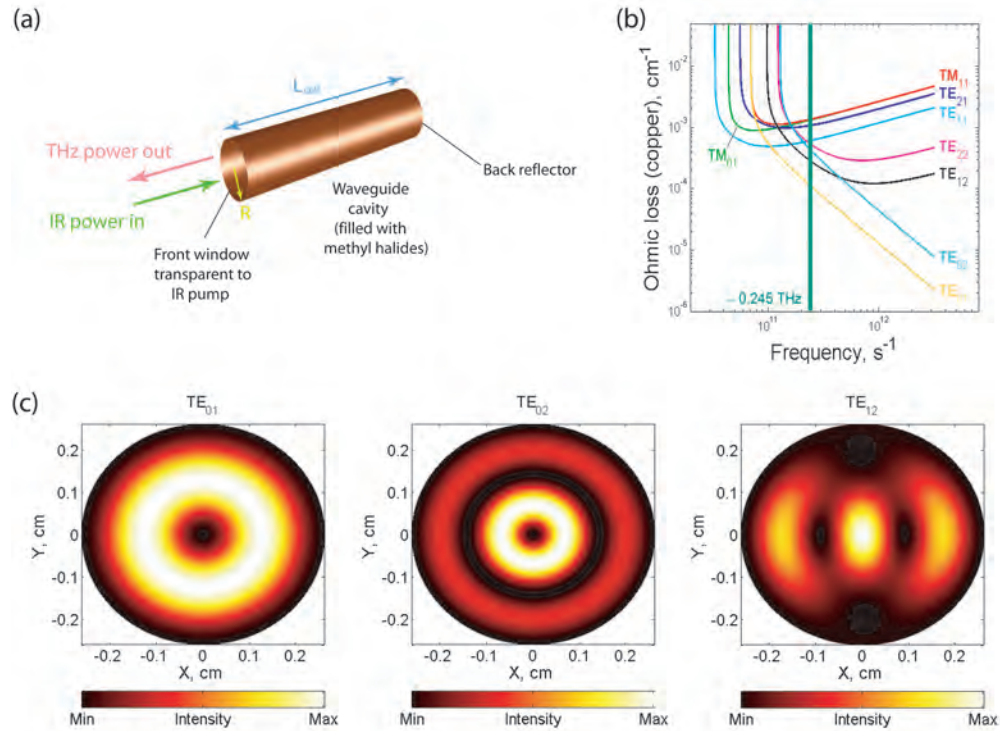
Fig. 2. (a) The OPFIR laser system considered in our numerical modeling: A cylindrical waveguide resonator of length L_{cell} and radius R is filled with a suitable gas that lases at the desired THz frequency, while pump power at a much higher IR frequency enters the system from the front window. In our example, $^{13}CH_3F$ is pumped with CO_2 laser at 31 THz to produce lasing at 0.245 THz. (b) Frequency dependence of the ohmic losses for the five lowest order modes (i.e. TE_{11}, TM_{01}, TE_{21}, TE_{01}, TM_{11}) and three higher order ones with low losses (i.e. TE_{02}, TE_{12}, TE_{22}). Plot is for a copper cavity with $R = 0.26\ cm$ (and assuming $L_{cell} \gg R$) so that several modes (not all shown in plot) have cut-offs below the THz lasing frequency. Despite this, only the lowest loss mode TE_{01} exist in the cavity near the lasing threshold. Vertical green line shows the band of frequency at which our system operates. (c) Intensity profile of the three lowest loss modes supported by the $R = 0.26\ cm$ waveguide cavity.

tional levels, $J_{v_0} = 3,4,5$ in the ground vibrational state and $J_{v_3} = 4,5,6$ in the excited state, are included (see detailed rate equations in the Appendix). Here, the K-swap processes occur at roughly 1-2 times the rates of the rotational transitions, and through this process, the lower and higher adjacent J levels can be modeled as part of their respective pool. For low pressure operation, we include the doubly degenerate v_6 state as our only higher excited vibrational state. As we shall see next, these relatively small number of rotational-vibrational levels are already sufficient to attain reasonable match between numerical predictions and experimental data. The system is uniformly pumped at room temperature ($T = 300\ K$) with CW CO_2 laser at 31 THz in which molecules are excited between $J_{v_0} = 4$ and $J_{v_3} = 5$ to produce primary lasing transition at 0.245 THz in $J_{v_3} = 4 - 5$ of the v_3 vibrational state, with τ_{spont} roughly chosen to be $15s$ [19]. It is also noted that the occupancy of v_3 is comparatively low $\left(f = e^{-E_v/kT} \approx 1/150\right)$, making the condition favorable for the creation of population inversion between $J_{v_3} = 5$ and the

level immediately below. Lastly, K_i in Fig. 1 equals 3 for $^{13}CH_3F$ and we have approximated the K-swap process as the faster $\Delta K=3n$ process where the V-swap rate is slow and primarily equilibrates A and E states in the pool. Other molecules with a slower or absent $\Delta K=3n$ process will need to approximate the K-swap process by the V-swap process. The rate constants and other salient molecular parameters used are provided in the Appendix.

Figure 2(b) shows a plot of the ohmic losses in a $R = 0.26$ cm copper waveguide cavity as a function of frequency. This loss prediction is made assuming $L_{cell} \gg R$ so that only the circular plane of the cavity matters and that the copper conductivity is high enough that the wall currents flow uniformly within a skin depth of the surface [18]. At the operating frequency, shown as a green vertical band in figure, the cavity supports multiple modes but only the five lowest order modes and three higher order ones that have low ohmic losses are included in the plot. The cut-off frequency of each of these modes can also be deduced from the figure. The lowest loss mode, TE_{01}, will be the first to lase upon threshold and remains the only mode present for pump power near the threshold, despite the cavity's ability to support multiple modes at THz. Alternatively, one can ensure single-mode operation even for large pump power by selecting the smallest possible cavity size with radius $\sim \lambda_{THz}/2$, where λ_{THz} is the wavelength of the THz lasing output. For our purpose, it suffices to simply operate near the threshold for single-mode operation since this also facilitates independent design optimizations of our system based on molecular gas physics and photonics considerations. Figure 2(c) depicts the intensity profiles of the three lowest loss modes of the cavity. It may be noted that the magnitude of ohmic loss scales roughly with the fraction of modal intensity residing near the cell wall, which in turn relates to the amount of penetration, to within a skin depth, into the wall. At low enough pump rate, only losses of TE_{01} mode (both ohmic losses and leakage through the end mirrors) can be compensated by the gain produced in $^{13}CH_3F$ while the other modes remain suppressed. Thus, we shall consider TE_{01} to be the lowest-threshold lasing mode.

Figure 3 plots typical spatio-temporal results of the numerical simulation. In particular, the evolution of the laser transition $\Delta N(\lambda_{THz})$ and the v_3 thermal pool to steady state are presented and compared at 250 and 350 mTorr, assuming P_{pump} to be 10 watts in CW operation. A few initial observations are in order: *(i)* the radial spatial profile of $\Delta N(r)$ is the inverse of that for v_3 pool. This is the pool quenching that leads to the vibrational bottleneck mentioned earlier. Note the rapid removal of molecules from v_3 near the cell wall is critical to maintaining the inversion. *(ii)* The cell center takes a long time to attain steady state given that the wall rate is slow far away from the wall (i.e. molecules have to travel a long distance to reach the cell boundary). *(iii)* Similarly, a longer time is required to reach steady state at a higher pressure due to the decreased k_{wall} near the cell center. In Fig. 3, steady state is attained after 100 μs at 250 mTorr while it takes 300 μs to do so at 350 mTorr. *(iv)* The magnitude of the variation across the radial direction of the cavity is greater at higher pressure, as will be explained shortly. While we mostly deal with CW systems in this paper, the ability to track the full temporal development of the laser action allows pulsed systems to be studied as well.

We next verify our numerical model against experimental results for a $R = 0.26$ cm copper cavity $^{13}CH_3F$ laser. The experimental configuration was identical to that described in [6], with a 1 mm diameter output coupler hole in the front reflector through which the IR pump and THz laser power were transmitted [Fig. 2(a)]. The slope efficiency was measured as the ratio of the THz laser power emitted to the corresponding IR pump intensity, and the threshold pump intensity was the extrapolation of this slope to zero THz power. Numerical predictions and experimental measurements of both the pump power and slope efficiency at threshold are compared at two pressures: 100 mTorr and 300 mTorr. Here, we adopt a semi-analytic approach for these comparisons, where knowledge of the losses in the OPFIR system and population inversions calculated with our model are used simultaneously. In the following, we first discuss
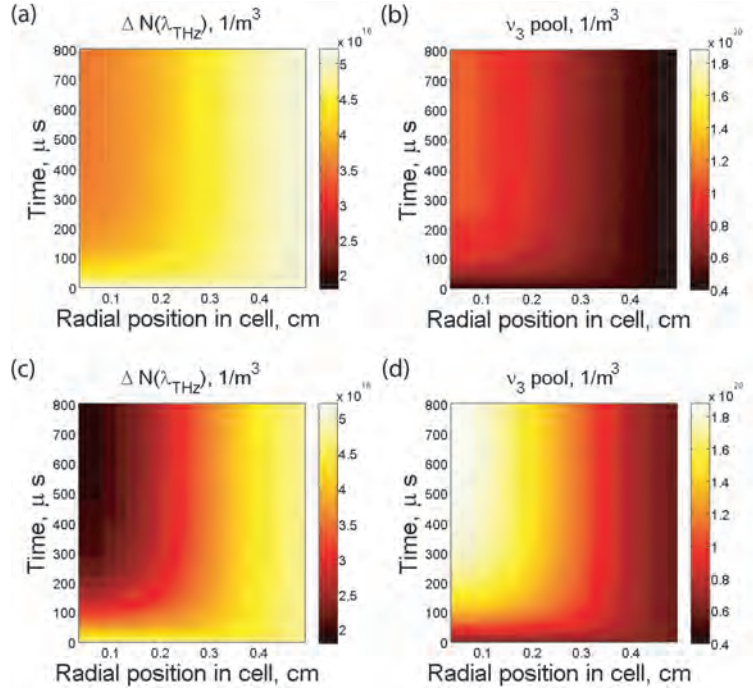
Fig. 3. Time dependent properties of laser system with CW pumping at $P_{\text{pump}} = 10$ W. (a) Time evolution of the inversion in v_3 state at 250 mTorr across the radial axis of the cavity until steady state behavior is observed. (b) Time evolution of the v_3 thermal pool population at 250 mTorr across the radial axis of the cavity until steady state behavior is observed. (c) Same as in (a) except operated at 350 mTorr (using the same magnitude range for the color bar). (d) Same as in (b) except operated at 350 mTorr (using the same magnitude range for the color bar).

the match for the threshold power intensity before addressing that of the slope efficiency.

The blue lines in Figs. 4(a) and 4(b) depict the unsaturated effective gain values of the system, as predicted by our model, for a range of pump intensity at 100 and 300 mTorr respectively. The gain for the $J = 4 - 5$ lasing transition in v_3 state of $^{13}\text{CH}_3\text{F}$ may be written as [20, 21]

$$\langle \gamma(\lambda_{\text{THz}}) \rangle = \langle \Delta N \rangle \frac{\lambda_{\text{THz}}^2}{4\pi^2 n^2 \tau_{\text{spont}} \Delta v(\lambda_{\text{THz}})} \quad (3)$$

where $\langle \Delta N \rangle$ is the pressure-dependent steady-state effective inversion defined as

$$\langle \Delta N(t_\infty) \rangle = \frac{\int_{V_{\text{ACT}}} d\mathbf{r} \, |\mathbf{E}_0(\mathbf{r})|^2 \, \Delta N(\mathbf{r}, t_\infty)}{\int_{V_{\text{ACT}}} d\mathbf{r} \, |\mathbf{E}_0(\mathbf{r})|^2}. \quad (4)$$

$\mathbf{E}_0(\mathbf{r})$ is the normalized mode profile of the passive cavity ($\int d\mathbf{r} \, \varepsilon_0 \, n^2(\mathbf{r}) \, |\mathbf{E}_0(\mathbf{r})|^2 = 1$) and V_{ACT} being the volume of active region of the considered structure. In our case, V_{ACT} is the entire cavity (note that this implies that the gas's behavior is less relevant in regions where the modal intensity is small but plays an important role in regions of high field intensity). In the considered case, $\Delta N(\mathbf{r}) = N_{\text{tot},J=5}^{v_3}(\mathbf{r}) - g_{J=4}^{v_3} N_{\text{tot},J=4}^{v_3}(\mathbf{r})/g_{J=5}^{v_3}$ with $N_{\text{tot},J}^{v_3}$ being the *total* molecular density of the upper ($J = 5$) and lower ($J = 4$) lasing transition level in v_3 state after accounting for the fractional contribution from the excited thermal pool, and $g_J^{v_3} = 2J + 1$ is the degeneracy

of the excited state's J^{th} level. $\mathbf{E}_0(\mathbf{r})$ is the normalized field of the TE_{01} mode and $n \approx 1$ for the gas. The width of the transition line, $\Delta \nu$, is broadened due to a combination of Doppler effects and molecular collisions and has a strong dependence on both pressure and transition frequency. The former is associated with the Gaussian lineshape while the latter, which leads to pressure broadening, is Lorentzian. Hence, $\Delta \nu = (\Delta \nu_D^2 + \Delta \nu_P^2)^{1/2}$ where the two terms are the Doppler and pressure broadening widths respectively, and the overall lineshape function used is the one that corresponds to the larger broadening parameter of the two. It is noted that for the same half width, pressure-broadened lines are stronger far away from the line-center than the Doppler-broadened ones. The gain defined in Eq. (3) accounts for the number of modes only in the frequency interval $\nu_{THz} \pm \Delta \nu / 2$ by assuming a large optical resonator whose dimension is several wavelengths so that its exact shape becomes less significant. We find that this applies in our case since the cylindrical copper waveguide is almost $100\lambda_{THz}$ long and a few λ_{THz}s in diameter. Moreover, the inversion density, and hence gain, is not saturated by stimulated emission for the entire range of input intensity plotted. As we are only interested in the threshold value in this part of the work, such approach remains valid.

The threshold for lasing may be approximated (neglecting spontaneous emission) to occur when the gain balances the total losses of the OPFIR system. Losses in our setup are assumed to be due to either ohmic losses from the E-field penetration into the copper wall or to energy leakage from the front mirror. For $L_{cell} \gg R$, we can treat the system as one-dimensional along the cylinder axis for loss analysis and quantify its coefficient as $2\alpha_{ohmic} - \ln(\Gamma_{front}\Gamma_{back})/L_{cell}$, where α_{ohmic} is the amplitude loss coefficient shown in Fig. 2(b). The magnitudes of these loss coefficients are indicated as horizontal red lines in Figs. 4(a) and 4(b). As such, the input threshold intensity predicted from our model is determined at the intersection between the red and blue lines, which indicates the point at which losses are compensated by the gain at λ_{THz} so that any further increase in pump intensity saturates the gain and is thereby channeled into coherent output power that escapes from the front window. From Figs. 4(a) and 4(b), the numerical thresholds attained are 0.78 and 2.42 W/cm^2 for the laser operated at 100 mTorr and 300 mTorr, respectively.

To make realistic comparisons with experiment, the decreasing absorption of the IR pump beam as it propagates along the cavity has to be considered. The pressure-dependent IR absorption coefficient, α', for $^{13}CH_3F$ is 71 m^{-1}Torr^{-1} [14] so that the ability of the pump to excite the gas decreases with increasing pressure. The effect is to reduce the amount of IR power effectively pumping the gas and can be captured by defining an incident pump power $P_{pump}^{inc} = P_{pump}/\kappa$, where κ is a pressure-dependent factor that accounts for the net fraction of incident IR power available for excitation in the L_{cell} long cavity. This factor is simply given by $(1/L_{cell}) \times \int_0^{L_{cell}} e^{-\alpha' x} dx$. Hence, $\kappa = 0.67$ and 0.36 for our 100 mTorr and 300 mTorr setups resulting in actual pump thresholds $(P_{pump}^{inc}/\pi R^2)$ of 1.2 and 6.7 W/cm^2, respectively. These results compare well with experimentally measured thresholds of 1.1 ± 0.4 and 5.5 ± 1.5 W/cm^2. Possible sources of discrepancy in the comparison include instabilities that make measuring the threshold difficult, deviation from spatially uniform pumping in the experiment, the one-dimensional treatment in balancing gain-loss, and the possibility that the emission was from the refilling transition in the ν_0 state. Even so, the current treatment provides adequately accurate predictions of the lasing thresholds. More importantly, this comparison acts to verify our claim that the aforementioned model of the OPFIR is physically robust and rigorous, yet numerically tractable.

Next, we present a similar comparison for the slope efficiency at threshold using a semi-analytic approach. The set of rate equations in Eq. (1), with the inclusion of the induced lasing transition rate, are solved analytically at steady-state to obtain the following approximate rela-
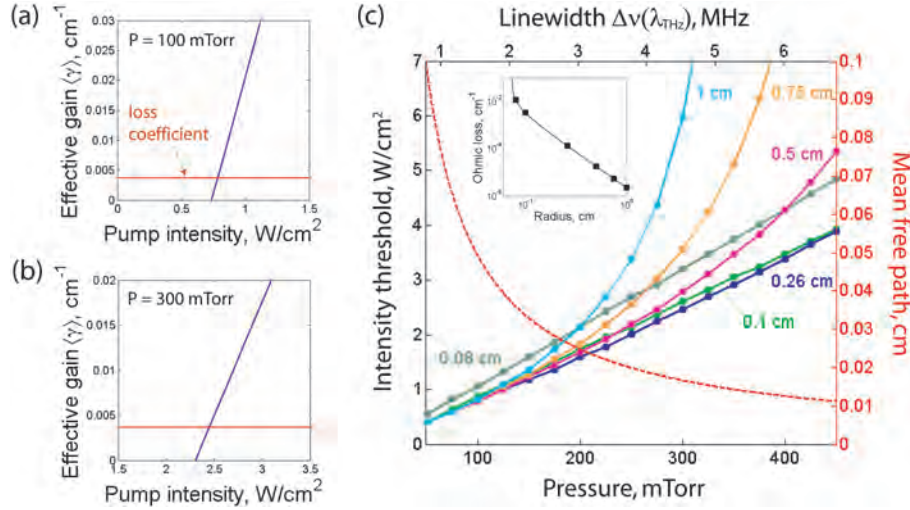
Fig. 4. (a) Method of threshold predictions via gain-loss balancing used in plotting (c) for every pressure point. Here, we operate at 100 mTorr with $R = 0.26$ cm. The blue line is the unsaturated effective gain value for a range of pump intensity predicted by the aforementioned model while the red line is the magnitude of the loss coefficient due to absorption by the metallic cavity and energy leakage from the front window. Intersection between the two lines corresponds to the lasing threshold. (b) Same as in (a) except that the pressure is at 300 mTorr. (c) Left axis depicts the relationship between the threshold intensity and pressure for a range of R values from 0.08 cm to 1 cm as predicted from numerical model. The corresponding linewidth, $\Delta\nu$, of the lasing transition (over which it may be tuned) is also illustrated in the top axis. A general trend exists such that the lasing threshold increases with pressure. The right axis shows the mean free path, λ_{MFP}, within the gaseous system which at a fixed temperature, is inversely proportional to pressure. Inset is the ohmic loss [see Fig. 2(b)] of the TE_{01} mode at 0.245 THz, with the radii of interest marked as square markers.

tionship between output power P_{out} and input power P_{in} above threshold:

$$P_{\text{out}} = f_{\text{out}} P_{\text{sat}} \left(\frac{P_{\text{in}}}{P_{\text{in}}^{\text{th}}} - 1 \right) \tag{5}$$

where f_{out} accounts for the fraction of emitted power that escapes via the front window, and $P_{\text{in}}^{\text{th}}$ is the IR power at threshold. P_{sat} is the saturation power at THz in which the gain in the system is half its unsaturated value. In this particular system, $P_{\text{sat}} = \hbar\omega_{\text{THz}} \int_{V_{\text{ACT}}} d\mathbf{r} \Delta N_{\text{th}}(\mathbf{r}) / \tau_{\text{eff}}$ where ΔN_{th} is the inversion at threshold and τ_{eff} is an effective lifetime that accounts for the various rates between the rotational levels in the lasing ν_3 state, and is found to be

$$\tau_{\text{eff}} = \frac{1/\tau_{J_1}^{\text{swap}} - 1/\tau'}{1/\tau_{J_1}^{\text{swap}} \tau_{J_2,J_1} - 1/\tau' \tau_{J_1}} \tag{6}$$

with

$$\frac{1}{\tau'} = \frac{\tau_{J_3} - \tau_{J_3,J_2} - \tau_{J_2,J_3} \tau_{J_3,J_2} / \tau_{J_2}^{\text{swap}}}{\tau_{J_2,J_3} \tau_{J_3,J_2}},$$

$$\frac{1}{\tau_{J_1}} = \frac{1}{\tau_{J_1,J_2}} + \frac{1}{\tau_{J_1}^{\text{swap}}} \quad \text{and} \quad \frac{1}{\tau_{J_3}} = \frac{1}{\tau_{J_3,J_2}} + \frac{1}{\tau_{J_3}^{\text{swap}}}.$$

The lifetimes in Eq. (6) describe the transition rates in the excited ν_3 state where lasing occurs and are defined in accordance to their definitions in Fig. 1 and Eq. (1). With that, the slope $dP_{\text{out}}/dP_{\text{in}}$ is $f_{\text{out}}P_{\text{sat}}/P_{\text{in}}^{\text{th}}$. Using numerical results of ΔN_{th} and $P_{\text{in}}^{\text{th}}$ found from the full model and accounting for the pressure-dependent IR absorption discussed in the previous paragraph, we obtain a threshold slope efficiency of 24.5×10^{-6} and 39.2×10^{-6} at 100 mTorr and 300 mTorr, respectively. Note that the best slope efficiency for the considered $^{13}\text{CH}_3\text{F}$ laser is 8×10^{-3}, which is the Manley-Rowe limit when the quantum efficiency is 1. These calculated values compare reasonably well with experimental slope values of $(44 \pm 22) \times 10^{-6}$ and $(48 \pm 24) \times 10^{-6}$, for which the greatest source of uncertainty is the calibration of the the Golay cell used to detect the THz radiation. Given this, these results further validate our model.

We extend the threshold determination method of Figs. 4(a) and 4(b) to study how the threshold intensity behaves as both cell radius and pressure are varied in Fig. 4(c). A general trend exists such that the lasing threshold increases with pressure for every radius plotted. This can primarily be attributed to the fact that the linewidth, $\Delta\nu(\lambda_{\text{THz}})$, broadens with increasing pressure so that $\langle\gamma(\lambda_{\text{THz}})\rangle$ reduces [see Eq. (3)]. Note that the variation of the linewidth with pressure is captured in the top axis of the figure. Since the total loss of the system is pressure-independent, such gain reduction increases the threshold linearly with pressure for each value of R. Second order effects that further raise the threshold at high pressure originate from the vibrational bottleneck: A higher pressure impedes the molecular diffusion to the cell wall and the subsequent decrease in wall collision rates reduces the flow of molecules out of the the excited thermal pool, leading to enhanced absorption and hence, a weaker inversion $\langle\Delta N\rangle$ and gain. Equivalently, the same effects on $\langle\Delta N\rangle$ can be understood by recognizing that λ_{MFP} progressively makes up a smaller region near the cell wall as the pressure increases such that a greater proportion of the molecules are in the non-ballistic regime, which also leads to slower k_{wall}. Red dashed line plotted against the right axis depicts the pressure dependence of λ_{MFP}. Over the range of low pressures considered, the vibrational bottleneck is only observed for large radius cells (i.e. $R \geq 0.26$ cm in the current setup) while for smaller cavities, there is no vibrational bottleneck and the threshold dependence on pressure remains approximately linear.

From Fig. 4(c), it can also be seen that the threshold intensity increases with radius for R values larger than 0.26 cm but decreases with radius for R values smaller than 0.26 cm. To understand why $R = 0.26$ cm is nearly optimal, the reader is referred to the inset that illustrates the reduction in ohmic losses of the TE_{01} mode at 0.245 THz when R grows from the waveguide cut-off value, with the radii of interest examined in the main figure marked as square markers. For small radius, the ohmic loss is high and hence, possesses great influence on the direction of threshold shift. In this regime, when the radius increases, the corresponding fall in ohmic loss has the tendency to lower the threshold. On the other hand, at larger R values where the ohmic losses are low, the vibrational bottleneck increasingly raises or prevents threshold with increasing R and pressure. However, at pressures less than 100 mTorr in large cells (i.e. $R \geq 0.26$ cm), the pressure-dependent threshold lines in Fig. 4(c) converge to the linear behavior observed for cells with $R \leq 0.26$ cm. As we shall see next, this follows directly from the fact that λ_{MFP} grows large at low pressures, so for a constant intensity and pump rate R_{pump}, the inversion $\langle\Delta N\rangle$ and gain exhibit little radial dependence. As a result, variation of R has a much smaller effect on the wall collision rate, and correspondingly on $\langle\gamma\rangle$, at lower pressures. So, for cell radii where the ohmic losses are also low, the threshold remains almost unchanged as R is varied.

To understand the spatial effects on laser performance more clearly, the radial dependence of the inversion and gain in a $R = 0.5$ cm cavity pumped by CW CO_2 laser at $P_{\text{pump}} = 100$ W are studied in Fig. 5. From the intensity-weighted averaging scheme used in Eq. (4), we have already noted that it is most desirable to match the peak of the cavity's eigenmode intensity to regions where $\Delta N(r)$ or $\gamma(r)$ is maximum. Such consideration plays an important role in
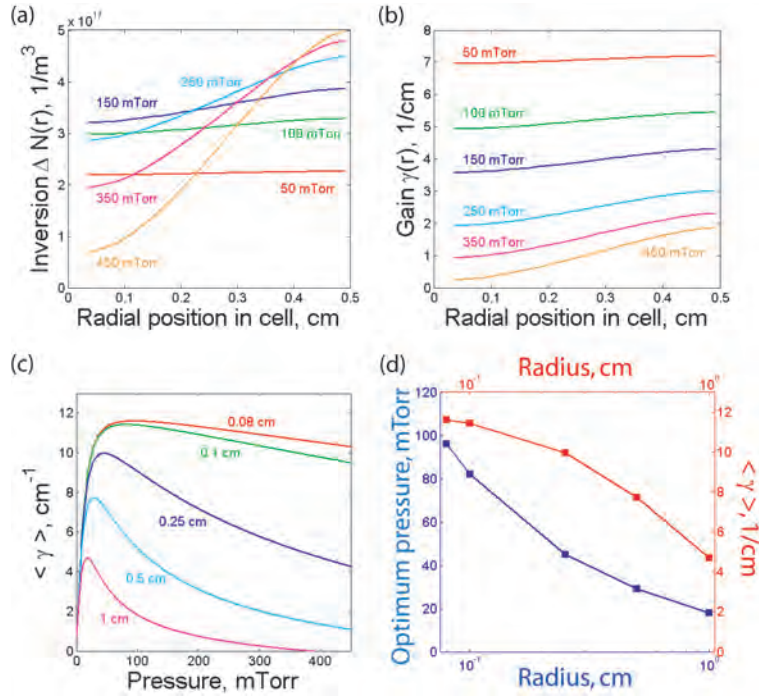
Fig. 5. (a) Radial spatial variation of the excited inversion in v_3 state of $^{13}CH_3F$ for a range of operating pressure from 50 to 450 mTorr. 0 cm marks the center of the cylindrical cavity while 0.5 cm marks the copper wall. All four panels in this figure assumed CW pumping at $P_{pump} = 100$ W. Near the cell wall, the diffusion is ballistic allowing significant reduction of molecules from the v_3 pool, and hence, results in a higher population inversion. (b) Same as in (a) except that the transition width at 0.245 THz is also factored in to study the gain. (c) Gain dependence on pressure for a fixed set of pump parameters. From a molecular gas physics standpoint, results clearly indicate that small R cavities are favored in terms of gain magnitude and pressure cut-off. (d) Data extracted from (c) where the left axis and right axis respectively depict the optimum operating pressure and the corresponding gain, as a function of cell radius R. Again, results here favored small sized cavity for high pressure operation.

designing the cavity itself. Figure 5(a) illustrates the distribution of $\Delta N(r)$ within the cavity for values of pressure ranging from 50 mTorr to 450 mTorr. In general, strong inversions are favored near the cell wall where the wall collision rates are the highest, and so, allow rapid depopulation of the excited and higher excited thermal pools to reduce pool quenching. This directly implies an advantage in exciting a lasing mode whose intensity peaks near the cell wall. However, such approach will also have to be weighted against the higher ohmic losses that arise from the field's enhanced interaction with the cell, in a similar trade-off effects to what was already discussed in Fig. 4(c). The details and treatment of the cavity design will be left for future work. We further note that the magnitude of radial variation in the cell increases with pressure. For instance, at 50 mTorr, a good proportion of the cavity is ballistic [see λ_{MFP} variation in Fig. 4(c)] so that ΔN is approximately uniform, i.e. $\Delta N(r_{cen}) = 0.96\Delta N(r_{wall})$ where r_{cen} and r_{wall} indicate the position at the cell center and wall, respectively. On the other hand, at 450 mTorr, most of the molecules are in the non-ballistic regime where $k_{wall} \propto 1/r^2$ as opposed to $k_{direct} \propto 1/r$. This leads to $\Delta N(r_{cen})$ to be only 14% of $\Delta N(r_{wall})$. Indeed, it was found that

the maximum inversion for the set of parameters used in this example increases with pressure because of the corresponding increase in N_{tot}. Figure 5(b) depicts a similar plot for the gain. The same characteristics are observed among the two except that $\gamma(r)$ is also influenced by the laser transition linewidth which broadens as pressure increases. This decrease of gain with pressure is again consistent with the discussion presented for Fig. 4(c), explaining why most OPFIR lasers use large diameter cavities operating at low pressure.

However, this design misses a critical point. Since R_{pump} increases when the same pump power is more tightly confined, the gain tends to grow as cavity radii shrink until it eventually saturates (because N_{tot} is a conserved quantity). Figures 5(c) and 5(d) track the optimum radius size for lasing based on the numerical model developed. An optimum operating pressure exists for each radius where the gain is maximized. Beyond that, vibrational bottleneck begins to play a dominant role, explaining the fall of the gain as pressure rises. At high enough pressure, the lasing action will be quenched. For example, in Fig. 5(c) the cut-off pressure occurs at 380 mTorr for $R = 1$ cm. Because of the role of higher lying vibrational levels, the cutoff pressure is pump intensity dependent such that the greater the pumping intensity, the higher the cut-off pressure. Thus, the optimum pressure and gain results summarized in Fig. 5(d) based on the molecular gas physics greatly favor small-sized cavities, especially if the effects of waveguide ohmic losses can be overcome.

4. Conclusions

We have presented a comprehensive theoretical analysis of lasing action in optically-pumped rotationally excited molecular gases confined in a metallic cavity. In order to do that, we have developed a theoretical framework that provides a realistic spatio-temporal description of the molecular de-excitation and diffusion processes occurring inside the cavity. Our approach also accounts for the influence on the main laser features of the electric-field intensity distribution and the ohmic losses associated to the different cavity modes. To illustrate this theoretical framework, we have analyzed in detail the case of lasing action from optically-pumped methyl fluoride gas confined in a cylindrical copper cavity. Our simulations have shown that for this system, the region of maximum population inversion is located near the cavity walls. The outcome of our calculations has also shown that the lowest lasing threshold mode corresponds to the cavity mode whose electric-field intensity profile presents an optimal spatial overlap with the corresponding population inversion distribution inside the cavity, and at the same time, minimizes the ohmic losses at the lasing frequency. Furthermore, we have predicted the existence of an optimal radius, determined by the interplay between the overall gain in the system and the corresponding ohmic losses, which minimizes the lasing threshold intensity for a large interval of gas pressures. We believe the results reported in this paper could contribute to the development of a novel class of room-temperature compact sources of far-infrared and THz radiation.

Appendix: Rate equations and rate constants of $^{13}CH_3F$ gas lasers

In this appendix, we first present the set of rate equations used to model the $^{13}CH_3F$ gas lasers. Figure 6 and Eq. (7) to Eq. (15) refer to a specific example of a methyl fluoride gas discussed in Sec. 3, adopted from the general model presented in Fig. 1, Eq. (1) and Eq. (2) of Sec. 2. We have labeled the rotational levels from N_1 to N_6, and the thermal pools as N_A, N_B and N_C. Hence, τ_{12}, τ_{23}, τ_{45}, τ_{56}, and their reverse processes represent rotational transitions due to dipole-dipole collisions, τ_{1A}, τ_{4B}, and similar processes represent K-swap transition lifetimes from the rotational levels (i.e. N_1 and N_4) into their respective thermal pools (i.e. N_A and N_B), and τ_{AB}, τ_{AC}, and their reverse processes are vibrational transitions which arise due to collisions with the cell wall. Readers should note that all notations in the main body of the paper are kept
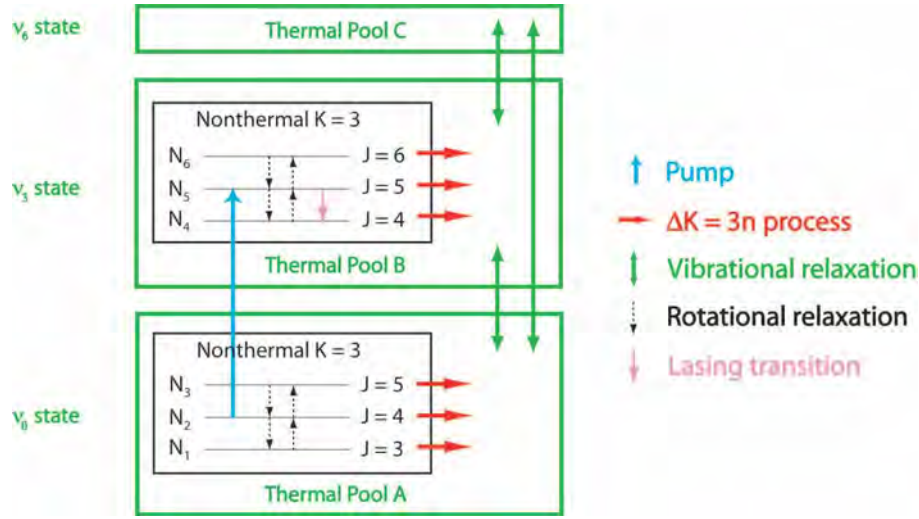
Fig. 6. $^{13}CH_3F$ OPFIR laser model used in this paper: results of diagnostic studies and theoretical considerations restrict the degrees of freedom so that a numerically tractable, yet physically accurate model is attained. Details on each process labeled are described in the text.

consistent with those used in Fig. 1, Eq. (1) and Eq. (2).

$$\frac{\partial N_1(\mathbf{r},t)}{\partial t} = -N_1(\mathbf{r},t)\left(\frac{1}{\tau_{12}}+\frac{1}{\tau_{1A}}\right)+\frac{N_2(\mathbf{r},t)}{\tau_{21}}+D\nabla^2 N_1(\mathbf{r},t) \tag{7}$$

$$\frac{\partial N_2(\mathbf{r},t)}{\partial t} = -N_2(\mathbf{r},t)\left(\frac{1}{\tau_{21}}+\frac{1}{\tau_{23}}+\frac{1}{\tau_{2A}}\right)+\frac{N_1(\mathbf{r},t)}{\tau_{12}}+\frac{N_3(\mathbf{r},t)}{\tau_{32}}$$
$$+R_{\text{pump}}(\mathbf{r},t)\Delta N_{\text{pump}}(\mathbf{r},t)+D\nabla^2 N_2(\mathbf{r},t) \tag{8}$$

$$\frac{\partial N_3(\mathbf{r},t)}{\partial t} = -N_3(\mathbf{r},t)\left(\frac{1}{\tau_{32}}+\frac{1}{\tau_{3A}}\right)+\frac{N_2(\mathbf{r},t)}{\tau_{23}}+D\nabla^2 N_3(\mathbf{r},t) \tag{9}$$

$$\frac{\partial N_4(\mathbf{r},t)}{\partial t} = -N_4(\mathbf{r},t)\left(\frac{1}{\tau_{45}}+\frac{1}{\tau_{4B}}\right)+\frac{N_5(\mathbf{r},t)}{\tau_{54}}+D\nabla^2 N_4(\mathbf{r},t) \tag{10}$$

$$\frac{\partial N_5(\mathbf{r},t)}{\partial t} = -N_5(\mathbf{r},t)\left(\frac{1}{\tau_{54}}+\frac{1}{\tau_{56}}+\frac{1}{\tau_{5B}}\right)+\frac{N_4(\mathbf{r},t)}{\tau_{45}}+\frac{N_6(\mathbf{r},t)}{\tau_{65}}$$
$$-R_{\text{pump}}(\mathbf{r},t)\Delta N_{\text{pump}}(\mathbf{r},t)+D\nabla^2 N_5(\mathbf{r},t) \tag{11}$$

$$\frac{\partial N_6(\mathbf{r},t)}{\partial t} = -N_6(\mathbf{r},t)\left(\frac{1}{\tau_{65}}+\frac{1}{\tau_{6B}}\right)+\frac{N_5(\mathbf{r},t)}{\tau_{56}}+D\nabla^2 N_6(\mathbf{r},t) \tag{12}$$

$$\frac{\partial N_A(\mathbf{r},t)}{\partial t} = -N_A(\mathbf{r},t)\left(\frac{1}{\tau_{AB}(\mathbf{r})}+\frac{1}{\tau_{AC}(\mathbf{r})}\right)+\frac{N_B(\mathbf{r},t)}{\tau_{BA}(\mathbf{r})}+\frac{N_C(\mathbf{r},t)}{\tau_{CA}(\mathbf{r})}$$
$$+\frac{N_1(\mathbf{r},t)}{\tau_{1A}}+\frac{N_2(\mathbf{r},t)}{\tau_{2A}}+\frac{N_3(\mathbf{r},t)}{\tau_{3A}}+D\nabla^2 N_A(\mathbf{r},t) \tag{13}$$

$$\frac{\partial N_B(\mathbf{r},t)}{\partial t} = -N_B(\mathbf{r},t)\left(\frac{1}{\tau_{BA}(\mathbf{r})}+\frac{1}{\tau_{BC}}\right)+\frac{N_A(\mathbf{r},t)}{\tau_{AB}(\mathbf{r})}+\frac{N_C(\mathbf{r},t)}{\tau_{CB}}$$
$$+\frac{N_4(\mathbf{r},t)}{\tau_{4B}}+\frac{N_5(\mathbf{r},t)}{\tau_{5B}}+\frac{N_6(\mathbf{r},t)}{\tau_{6B}}+D\nabla^2 N_B(\mathbf{r},t) \tag{14}$$
$$\frac{\partial N_C(\mathbf{r},t)}{\partial t} = -N_C(\mathbf{r},t)\left(\frac{1}{\tau_{CA}(\mathbf{r})}+\frac{1}{\tau_{CB}}\right)+\frac{N_A(\mathbf{r},t)}{\tau_{AC}(\mathbf{r})}+\frac{N_B(\mathbf{r},t)}{\tau_{BC}}$$
$$+D\nabla^2 N_C(\mathbf{r},t) \tag{15}$$

where $\Delta N_{\text{pump}}(\mathbf{r},t)=N_5^{\text{tot}}(\mathbf{r},t)-g_5 N_2^{\text{tot}}(\mathbf{r},t)/g_2$ with $N_2^{\text{tot}}(\mathbf{r},t)$ being the *total* molecular density of $J=4$ nonthermal level in v_0 state after accounting for the fractional contribution from thermal pool A, and $g_2=9$ is its degeneracy. Similar definitions hold for N_5^{tot} and $g_5=11$.

Table 1 provides the rate constants and relevant molecular parameters used in our calculations [8, 14, 15].

Table 1. Translational Cross Sections (in $\mathring{A}^2$) of ^{13}CH$_3$F

Mass (AMU)	35
Gas kinetic collision cross section	44
$v_3 \rightarrow v_6$ cross section at 300 K, σ_{exc}	2.65
Dipole-dipole cross section at 300 K, σ_{DD}	320
K-swap cross section at 300 K, $\sigma_{\text{K-swap}}$	137